batteries

MDPI

Article

Functionalization of Cathode–Electrolyte Interface with Ionic Liquids for High-Performance Quasi-Solid-State Lithium–Sulfur Batteries: A Low-Sulfur Loading Study

Milinda Kalutara Koralalage [1,†], Varun Shreyas [2,†], William R. Arnold [2], Sharmin Akter [2], Arjun Thapa [3], Badri Narayanan [2,3,*], Hui Wang [2,3], Gamini U. Sumanasekera [1,3,*] and Jacek B. Jasinski [3,*]

[1] Department of Physics and Astronomy, University of Louisville, Louisville, KY 40292, USA
[2] Department of Mechanical Engineering, University of Louisville, Louisville, KY 40292, USA
[3] Conn Center for Renewable Energy Research, University of Louisville, Louisville, KY 40292, USA
* Correspondence: badri.narayanan@louisville.edu (B.N.); gamini.sumanasekera@louisville.edu (G.U.S.); jacek.jasinski@louisville.edu (J.B.J.)
† These authors contributed equally to this work.

Abstract: We introduce a quasi-solid-state electrolyte lithium-sulfur (Li–S) battery (QSSEB) based on a novel Li-argyrodite solid-state electrolyte (SSE), Super P–Sulfur cathode, and Li-anode. The cathode was prepared using a water-based carboxymethyl cellulose (CMC) solution and styrene butadiene rubber (SBR) as the binder while $Li_6PS_5F_{0.5}Cl_{0.5}$ SSE was synthesized using a solvent-based process, via the introduction of LiF into the argyrodite crystal structure, which enhances both the ionic conductivity and interface-stabilizing properties of the SSE. Ionic liquids (IL) were prepared using lithium bis(trifluoromethyl sulfonyl)imide (LiTFSI) as the salt, with pre-mixed pyrrolidinium bis(trifluoromethyl sulfonyl)imide (PYR) as solvent and 1,3-dioxolane (DOL) as diluent, and they were used to wet the SSE–electrode interfaces. The effect of IL dilution, the co-solvent amount, the LiTFSI concentration, the C rate at which the batteries are tested and the effect of the introduction of SSE in the cathode, were systematically studied and optimized to develop a QSSEB with higher capacity retention and cyclability. Interfacial reactions occurring at the cathode–SSE interface during cycling were also investigated using electrochemical impedance spectroscopy, cyclic voltammetry, and X-ray photoelectron spectroscopy supported by ab initio molecular dynamics simulations. This work offers a new insight into the intimate interfacial contacts between the SSE and carbon–sulfur cathodes, which are critical for improving the electrochemical performance of quasi-solid-state lithium–sulfur batteries.

Keywords: quasi-solid-state electrolyte Li–S battery; carbon–sulfur cathodes; ionic liquids; cathode–SSE interface

check for updates

Citation: Koralalage, M.K.; Shreyas, V.; Arnold, W.R.; Akter, S.; Thapa, A.; Narayanan, B.; Wang, H.; Sumanasekera, G.U.; Jasinski, J.B. Functionalization of Cathode–Electrolyte Interface with Ionic Liquids for High-Performance Quasi-Solid-State Lithium–Sulfur Batteries: A Low-Sulfur Loading Study. *Batteries* **2024**, *10*, 155. https://doi.org/10.3390/batteries10050155

Academic Editors: Peter Mahon and Can Liao

Received: 13 March 2024
Revised: 23 April 2024
Accepted: 25 April 2024
Published: 30 April 2024

Copyright: © 2024 by the authors. Licensee MDPI, Basel, Switzerland. This article is an open access article distributed under the terms and conditions of the Creative Commons Attribution (CC BY) license (https://creativecommons.org/licenses/by/4.0/).

1. Introduction

With the rapid increase in the demand for energy storage devices, it has been challenging to meet the desired standards and specifications such as energy density, cycle stability, and cost, utilizing the conventional Lithium-ion batteries [1–4]. Lithium–Sulfur (Li–S) batteries, on the other hand, stand to be one of the most promising candidates to meet the energy storage requirement for electric vehicles and portable storage devices, with their natural abundance of materials, high theoretical capacity of 1672 $mAhg^{-1}$, high energy density of 2600 $Whkg^{-1}$, low cost, and lower impact to the environment [5–8]. During the discharge process of the Li–S battery, Li^+ ions produced at the anode migrate through the electrolyte towards the cathode while electrons move through the external circuit, producing polysulfides and Li_2S at the cathode as the final discharge products [9,10].

However, there are some challenges that need to be addressed in the applications of Li–S batteries. Sulfur itself, Li_2S_2, and Li_2S are electrical insulators which reduce the

active material utilization and electronic conductivity of the cathode, affecting the battery performance [11]. Combinations of different carbon materials such as graphene, mesoporous carbon, carbon nanotubes, etc., with sulfur in the cathode electrode have been utilized, aiming to overcome the conductivity reduction due to the insulating nature of sulfur and polysulfides, as well as to address the polysulfide volume expansion during lithiation [12–16].

Polysulfides formed while charging and discharging easily dissolve in liquid electrolyte and polysulfide shuttling leads to poor coulombic efficiency and cyclability [17]. The liquid electrolytes used in conventional Li–S batteries flow easily and are flammable, giving rise to the safety concerns [18,19]. Lithium dendrites piercing through the separator causing short circuit paths is another major challenge which needs to be addressed. Replacement of the liquid electrolyte with a solid-state electrolyte (SSE) is one of the strategies to overcome the above-mentioned safety issues [20,21]. In an all-solid-state electrolyte battery (ASSEB), rapid ion migration is mainly accomplished through SSE. Consequently, it can effectively reduce the Li dendrite penetration to create short circuit paths by lowering the safety concerns. The absence of liquid electrolytes profoundly diminishes the polysulfide shuttle effect [22].

An all-solid-state Li–S battery is typically composed of a carbon–sulfur-based composite cathode, SSE, and a Li metal anode. When rigid SSE is used in the battery, there is a high chance of having a considerable mismatch at the interface with electrodes rising the interface resistance. In the literature, various approaches have been attempted to improve the SSE–cathode interface to have lower interfacial resistance to ion migration through the interface [23]. One way to improve the contact at the interface is to press the SSE onto the cathode under high pressure. Introducing a hybrid electrolyte consisting of SSE coupled with liquid electrolyte, polymer electrolyte or ionic liquid, is another approach to address the interfacial contact between the SSE and the electrodes [24–26]. With the presence of the liquid electrolyte in the discharge profile, a dual-phase plateau is expected in liquid electrolyte Li–S batteries at the cathode–liquid electrolyte interface (solid–liquid interface). The first part of the plateau, around 2.3 V, corresponds to the conversion of S_8 into Li_2S_4, which has an approximate theoretical capacity of around 418 $mAhg^{-1}$. The second phase of the discharge plateau at 2.1 V corresponds to further conversion of Li_2S_4 into the Li_2S and has potential to deliver a theoretical capacity around 1254 $mAhg^{-1}$. It should be emphasized that not all sulfur-cathodes undergo the two plateau discharge steps. The organic sulfur cathodes only show a solid-to-solid transition instead of a solid-to-liquid-to-solid transition. In the absence of the liquid electrolyte, which serves as the solvent for polysulfides, ASSEB also shows different reaction route that involves direct conversion between S_8 and Li_2S (solid-to-solid transition) without polysulfide formation at the cathode–SSE interface (solid–solid interface) [27]. This solid phase reaction shows the discharge plateau around 2.0 V. When both SSE and a small amount of ionic liquid are present simultaneously, both solid–liquid and solid–solid reactions take place. As a result, a mixed discharge profile is expected with multi-phase discharge plateaus. Batteries with such quasi-solid phase reaction are referred to as quasi-solid-state electrolyte batteries (QSSEB) [28].

Ionic liquid (IL)-based electrolytes are taken into consideration due to their high viscosity mitigating the solubility of sulfur and lithium polysulfides, thereby reducing the polysulfide shuttling effect. In the literature, there are a number of reports on ILs containing pyrrolidinium (PYR) as the cation and bis(trifluoromethyl sulfonyl)imide (TFSI) as the anion [29]. The major drawback of this IL is the low ionic conductivity and the high viscosity for high TFSI concentrations. To improve the conductivity and lower the viscosity, co-solvents have been introduced. The effects of co-solvents have been studied and optimized in previous reports. In this work 1,3-dioxolane (DOL) is used as the co-solvent to prepare the IL [30].

Different types of sulfur cathodes have been developed for Li–S liquid electrolyte batteries; however, the carbon–sulfur composite cathode stands out with the most effective outcomes, due to its higher electronic conductivity [31]. Various carbon–sulfur cathode

designs can be found in the literature, developed from graphene, carbon nanotubes, acetylene carbon black, etc. [32–36]. In this work, Super P conductive carbon black (SP) with an average pore volume of 0.14 cm^3g^{-1} and a surface area of 62 m^2g^{-1} [37] is used as the conductive carbon additive for sulfur cathode. The cathode consists of sulfur as the active material, Super P conductive carbon black and acetylene carbon black as the conductive carbon additive, and a water-based carboxymethyl cellulose (CMC) solution combined with premixed styrene butadiene rubber (SBR) as the binder.

Out of the various SSEs used for Li–S solid state batteries, sulfide-based solid electrolytes receive greater attention due to their higher ionic conductivity, compatible interface with sulfur-based cathodes, and lower grain boundary resistance [21,38]. Halogen-doped argyrodite solid electrolyte materials such as Li_6PS_5Cl have been extensively studied, but poor compatibility between SSE and the Li anode has hampered many efforts to use it in all-solid-state batteries [39]. Using a solvent-based process, $Li_6PS_5F_{0.5}Cl_{0.5}$ SSE was synthesized via the introduction of LiF into the argyrodite crystal structure, which affects both the ionic conductivity and interface-stabilizing properties of the SSE. Excess LiF from this halogen-doping technique creates an LiF-rich SEI layer which stabilizes the SSE/anode interface and effectively prevents Li dendrite formation [40]. The stabilizing influence of $Li_6PS_5F_{0.5}Cl_{0.5}$ combined with its impressive ionic conductivity of 3.5×10^{-4} S cm^{-1} makes it an excellent candidate to be used in a Li–S battery.

In this study, Li–S batteries consisting of SP–S-based composite cathodes, Li anodes and novel $Li_6PS_5F_{0.5}Cl_{0.5}$ SSE were tested with and without an IL at the electrode–SSE interfaces. Even though previous studies have reported ASSEBs consisting of sulfide-based SSEs, only a handful of them report the use of ILs to improve the interfacial contacts. Here, we report a comprehensive study of the choice of the IL, its optimum viscosity, and the volume needed to improve the solid–solid interfacial contacts influencing the interfacial reactions for improved cycle life of this novel QSSEB with the aid of ab initio molecular dynamics (AIMD) simulation studies. Special emphasis is given for a better understanding of interfacial reactions occurring at the cathode–SSE interface. This study focuses on a low-sulfur loading of 0.7 mg/cm^2, while research on high-sulfur loading of 4.0 mg/cm^2 is currently underway and will be presented in a follow-up paper.

2. Experimental

2.1. Materials and Chemicals

The following materials were acquired from their respective suppliers: Sulfur (Alfa Aesar, Haverhill, MA, USA 99.5%), Timcal graphite carbon super P (MTI, New York, NY, USA 98%), Carboxymethyl cellulose (MTI, New York, NY, USA 98%), pre-mixed Styrene butadiene rubber (40 w%), Acetylene Black (MTI, New York, NY, USA 98%), N,N-butylmethyl pyrrolidinium bis(triflouromethylsulfonyl)imide (TCI, Portland, OR, USA 98%), Lithium bis(triflouromethylsulfonyl)imide (Thermo Scientific, Waltham, MA, USA 99%), and 1,3-dioxolane (anhydrous 99% Sigma Aldrich, St. Louis, MI USA).

2.2. Super P–Sulfur Cathode Fabrication

Timcal graphite carbon super P and Sulfur were mixed in the ratio of (3:2) and Sulfur was infused by melt injection under vacuum at 115 °C for 2 h. Then, the mixture of Super P–Sulfur was mixed with acetylene black, 2.5% CMC dissolved in DI water, and SBR in the weight ratio of 90:2:4:4 to formulate the slurry. Next, the slurry was coated on aluminum current collector. After excess water was evaporated, electrodes were punched into 2.0 cm^2 disks and electrodes had a sulfur loading of 0.70 mgcm^{-2}. These electrodes were further dried under vacuum for 6 h at 50 °C before the battery assembly.

2.3. Solid State Electrolyte Synthesis

$Li_6PS_5F_{0.5}Cl_{0.5}$ solid electrolyte was synthesized via the stoichiometric mixing of lithium sulfide (Li_2S, Alfa Aesar), lithium chloride (LiCl, Alfa Aesar), lithium fluoride (LiF, Alfa Aesar), and β-Li_3PS_4 precursor in ethanol solvent and stirred for 1 h at room

temperature inside a glovebox under argon atmosphere. The solution was heated to evaporate the solvent before a subsequent heat treatment for 1 h at 200 °C. The resultant powder was collected and ground using mortar and pestle.

2.4. Ionic Liquid Preparation

All the ionic liquids were prepared inside the Argon-filled glove box and stored at room temperature. Relevant masses to prepare LiTFSI solutions (2 M and 4 M) were weighed and mixed with premixed PYR-TFSI and DOL (1:1 and 3:1) solvent for 48h.

2.5. Cathode Characterization

Thermo gravimetric analysis (TGA) studies of the cathode were carried out using a thermos gravimetric analyzer TA 2050 under N_2 gas flow of 100 mL/min. Cathode electrode surface morphology was characterized using the Field emission gun scanning electron microscope (FEI), and the TESCAN scanning electron microscope with energy dispersive X-ray spectroscopy (EDAX).

2.6. Battery Assembly

For the assembly of QSSEB, SP-S cathode with 0.70 mgcm^{-2} sulfur loading was punched into disks of 2.0 cm^2. SSE powder was pressed into 150 mg pellets using a stainless-steel tank. During the assembly, SSE was wetted with the relevant amounts of IL from both ends using a micropipette. Cathode, SSE, and Li metal anode were then assembled into 2032 type coin cell (Figure S1).

2.7. Electrochemical Testing

Electrochemical impedance spectroscopy (EIS) measurements of coin cells were carried out using the SP-200 electrochemical system, (BioLogic Science Instruments, Seyssinet-Pariset, France). Each spectrum was measured in the frequency range of 1 MHz to 50 mHz with an excitation voltage of 5 mV. Cyclic voltammetry measurements were also carried out using the same instrument at scan rate of 3 mV/min.

All the batteries were cycled at 30 °C between 1.0 V and 2.8 V using a 16 channel Arbin battery testing system.

2.8. X-ray Photoelectron Spectroscopy

X-ray photoelectron spectroscopy (XPS) (MultiLab 3000, VG Scientific, Sussex, UK) was employed to detect the chemical composition at the cathode–SSE interface after cycling. Prior to careful analysis, all the spectra were calibrated with respect to the C-C (sp2) binding energy (284.8 eV) of the C1s peak.

2.9. Ab Initio Molecular Dynamics Simulations

All AIMD simulations were performed within the framework of density functional theory (DFT) using projector augmented wave method as implemented in Vienna Ab initio Simulation Package (VASP) [40,41]. The exchange correlations were described using the Perdew–Burke–Ernzerhof (PBE) functionals within the generalized gradient approximation (GGA) using the pseudopotentials supplied by VASP: Li_sv (valence: $1s^2\ 2s^1\ 3p^0$), C (valence: $2s^2\ 2p^2$), F (valence: $2s^2\ 2p^5$), H (valence: $1s^1$), O (valence: $2s^2\ 2p^4$), N (valence: $2s^2\ 2p^3$), P (valence: $3s^2\ 3p^3$), S (valence: $3s^2\ 3p^4$), and Cl (valence: $3s^2\ 3p^5$). The energy cut off for plane wave basis-set is set at 500 eV. A Gaussian smearing of 0.05 eV was employed to treat the partial electron occupancies for each orbital. The Brillouin zone was sampled at the Γ-point only. For geometry relaxation.

The initial crystalline structures for two extreme charge states of cathode, namely Li_2S (fully discharged) and S_8 (fully charged) were obtained from Materials Project database [42]. These geometries were further optimized using DFT (at the PBE level of theory). Crystal structure for the bulk SSE ($Li_6PS_5F_{0.5}Cl_{0.5}$) was used from our previous study [43]. The computational supercells for the interfaces were constructed by stacking slabs of ionic

liquids: (1) 2 M LiTFSI in DOL/DME (1:1), (2) ([PYR14][TFSI]), and (3) 2 M LiTFSI in ([PYR14][TFSI])/DOL (1:1) on top of the SSE and cathodes (Li2S and S8). The simulation cell parameters are detailed in Table 1.

Table 1. Simulation lattice parameters for the interfaces considered in this study. All the interface models considered in this study are orthorhombic.

Ionic Liquid/Diluent	SSE/Cathode	Lattice Parameters (Å)		
		a	b	c
($[PYR_{14}][TFSI]$)	$Li_6PS_5F_{0.5}Cl_{0.5}$	10.186	10.186	28.636
	Li_2S	11.187	11.187	26.087
	S_8	10.559	12.945	38.170
DOL and DME (1:1)	$Li_6PS_5F_{0.5}Cl_{0.5}$	10.186	10.186	30.586
	Li_2S	11.187	11.187	27.387
	S_8	10.559	12.945	33.800
($[PYR_{14}][TFSI]$) and DOL (1:1)	$Li_6PS_5F_{0.5}Cl_{0.5}$	10.186	10.186	36.986
	Li_2S	11.187	11.187	30.150
	S_8	10.559	12.945	39.500

Prior to performing AIMD simulations, the as-constructed interface models were first relaxed at the PBE level of theory. For relaxation, the atomic coordinates and the lattice parameters were optimized such that the force on each atom was lower than 0.05 eV/Å. An energy convergence tolerance of 1×10^{-5}eV was employed for self-consistent field cycles, while the Brillouin zone was sampled using a $2 \times 2 \times 1$ Monkhorst-Pack *k*-grid. Thereafter, AIMD simulations were performed within a canonical ensemble (NVT) at 300 K for 20 ps using a timestep of 1 fs. For the AIMD simulations, we employed an energy convergence tolerance of 1×10^{-5}eV for the self-consistent field cycles, and a $1 \times 1 \times 1$ *k*-grid. Constant temperature conditions were maintained using a Nosé–Hoover thermostat as implemented in VASP. Long-range van der Waals dispersion interactions are treated using the zero damping DFT-D3 method of Grimme [44,45].

3. Results

3.1. Cathode Characterization

A TGA study of the cathode material was conducted using the thermo gravimetric analyzer TA 2050. Temperature was ramped at 10 °C/min from room temperature to 800 °C under Nitrogen flow of 100 mL/min. A cathode consisting of SP–S (3:2) 90 w% should have approximately 36% sulfur and it is confirmed from the TGA analysis, shown in Figure 1a, that the calculation of the loading based on the weight ratio is in excellent agreement. Figure 1b,c show the FEI SEM images obtained from the surface with magnifications 100 and 10,000, respectively. Surface porosity which led to high capacity and cyclability was clearly observable at higher magnification SEM images (Figure 1c). Figure 1d shows the cross-sectional SEM image obtained with 60° tilt angle with 2000 magnification in which the SP–S cathode coating has a thickness of ~50 µm. Figure 1e–g show the EDAX mapping obtained using TESCAN SEM on the cathode surface before cell assembly. The uniform distribution of carbon and sulfur, shown in Figure 1f,g, confirms that the injection of sulfur into the carbon matrix via the melt diffusion method was successful in this cathode fabrication process. A consistent and uniform distribution of sulfur in the cathode is needed for a higher active material utilization.

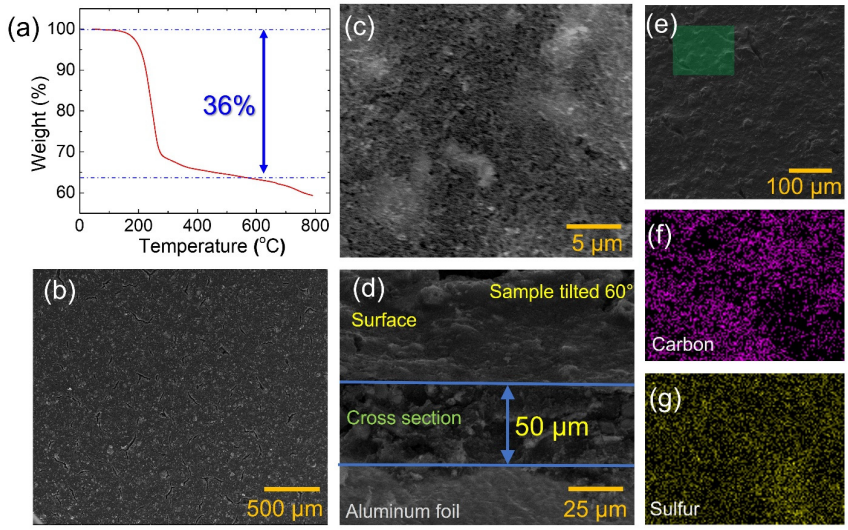

Figure 1. Cathode characterizations: (**a**) TGA measurement for quantifying active sulfur loading in cathode, FEI SEM image with (**b**) 100 and (**c**) 10,000 magnifications, (**d**) FEI SEM cross sectional image obtained with 60° tilt angle at 2000 magnification, (**e**) TESCAN SEM image for EDAX mapping, and (**f**) Carbon and (**g**) sulfur EDAX mapping.

3.2. Electrochemical Testing

Before discharging the cells, electrochemical impedance spectroscopy studies of a Li–S battery with and without IL functionalization were carried out. Figure 2a shows the Nyquist plots of the electrochemical impedance spectra of batteries consisting of the SP–S cathode, $Li_6PS_5F_{0.5}Cl_{0.5}$ SSE, and Li anode (i) without any ionic liquid (orange filled circles), (ii) with 40 μL of LiTFSI (1 M) dissolved in PYR (dark blue filled triangles), and (iii) with 40 μL of LiTFSI (2 M) dissolved in PYR/DOL (1:1) (green filled squares). As expected, the electrode–electrolyte interfacial resistance is seen to decrease significantly due to the introduction of the ionic liquid, as evidenced by the decrease in the charge transfer resistance and the electrolyte resistance. The first cycle discharge curves of all three cells presented in Figure 2b show a dramatic improvement in the discharge capacities with the addition of ionic liquid diluted with DOL.

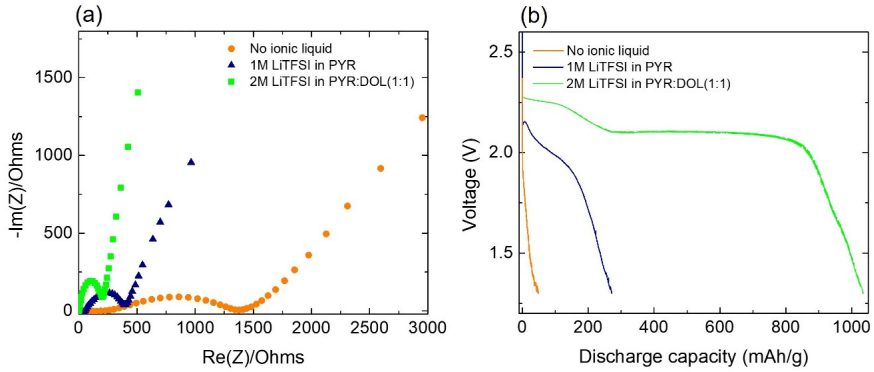

Figure 2. Electrochemical testing: (**a**) electrochemical impedance spectra and (**b**) discharge curves at 0.05 C rate for batteries with and without ionic liquids.

ASSEB assembled with the SP–S cathode, Li anode, and SSE (without any IL) showed only a poor initial discharge capacity (~42 mAh/g) (Figure 2b) without the ability to charge back, as anticipated from the EIS result (Figure 2a). Poor interfacial contact at the cathode–SSE and SSE–anode interface is believed to cause this poor performance. Next, 40 μL of IL consisting of LiTFSI (1 M) dissolved in PYR was introduced to both solid–solid interfaces to assemble the QSSEB. The assembled QSSEB was cycled at room temperature at C/20

(80 mA/g) current rate between 1.0 V and 2.8 V. QSSEB with LiTFSI (1 M) dissolved in PYR IL showed an initial discharge capacity of 337 mAh/g but decreased and stabilized at around 50 mAh/g after 100 cycles, as shown in Figure S2 in the Supplementary Materials. A discharge voltage plateau was observed around 2.1 V corresponding to the conversion of polysulfides (Li_2S_n, $2 < n < 8$) into solid lithium sulfides (Li_2S_2 and Li_2S). The decomposition of SSE and IL is believed to cause the rapid decrease in the capacity.

Due to the low initial discharge capacity of the Li–S batteries consisting of SP–S/SSE/Li, the highly viscous IL (LiTFSI in PYR) was diluted with 1,3-dioxolane (DOL) and LiTFSI content was kept constant at 1 M. Performance of the battery with LiTFSI (1 M) dissolved in PYR/DOL (1:1) is shown in Figure S3 in the Supplementary Materials. Even if the stability and cyclic performance were improved by the addition of the diluent, the initial capacity was still lower than expected (920 mAh/g). Due to this lower initial capacity, the concentration of LiTFSI in diluted PYR was increased to 2 M. The initial discharge capacity was seen to increase to > 1000 mAh/g, as shown in Figure 2b.

Figure 3a,b compare the battery performances with and without DOL in IL. Both batteries were tested at C/20 rate with IL volume of 40 µL at room temperature. The battery without the diluent (only PYR) and LiTFSI concentration of 0.6 M in PYR (best performance battery without diluent) shows an initial discharge capacity of ~600 mAh/g but fades to a value below 200 mAh/g after 100 cycles (Figure 3a). The battery with PYR/DOL (1:1) with 2 M concentration of LiTFSI shows a vastly improved initial discharge capacity of ~1100 mAh/g, still fading below 400 mAh/g after 100 cycles (Figure 3b).

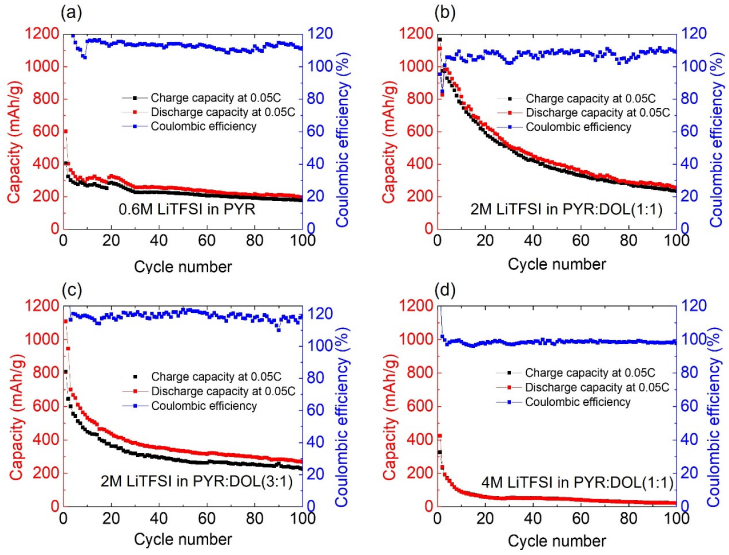

Figure 3. Performance of batteries consisting of SP–S/SSE/Li with ILs: (**a**) 0.6 M LiTFSI dissolved in PYR, (**b**) 2 M LiTFSI dissolved in PYR/DOL (1:1), (**c**) 2 M LiTFSI dissolved in PYR/DOL (3:1), and (**d**) 4 M LiTFSI dissolved in PYR/DOL (1:1).

Next, the battery performances at C/20 rate for varying diluent (PYR/DOL) ratios (1:1 and 3:1 PYR/DOL) were compared as shown in Figure 3b,c. Figure 3c shows the results for PYR/DOL ratio of 3:1. They both showed an initial discharge capacity of ~1100 mAh/g, still fading below 400 mAh/g after 100 cycles. A change in the PYR/DOL ratio did not have any noticeable difference in the initial discharge capacity or the retention capacity. However, the battery with a 1:1 ratio of PYR/DOL showed better coulombic efficiency at the tested C rate. Here, the coulombic efficiency was calculated using the ratio and the discharge capacity/charge capacity of a corresponding cycle. Based on these results, a PYR/DOL ratio of 1:1 was maintained during the rest of the work. In a comparison of the LiTFSI concentration on the battery performance with a PYR/DOL ratio of 1:1 and IL volume of 40 µL at C/20 rate, the battery with 4 M LiTFSI (Figure 3d) concentration showed much worse performance compared to 2 M concentration with the initial discharge

capacity of only ~400 mAh/g accompanied by a rapid degrading of the discharge capacity. This result confirmed again that the high viscosity of IL reduces the battery performance since 4 M LiTFSI IL was found to be highly viscous (130 mPa s^{-1}), similar to the IL without diluent (140 mPa s^{-1}), in comparison to the 2 M LiTFSI IL (24 mPa s^{-1}).

It was found that a 2 M LiTFSI concentration in a dilution of PYR with DOL at 1:1 ratio gives the optimum performance. In order to find the optimum volume of the IL required, we carried out a volume dependent battery performance study at C/20 rate, as shown in Figure 4, for the volumes of (a) 10 µL, (b) 20 µL, and (c) 40 µL. Both batteries with 40 µL and 20 µL (Figure 4b,c) ionic liquid volumes showed initial discharge capacities of ~1100 mAh/g, with capacity retention of ~300 mAh/g after 100 cycles. The battery with 40 µL IL volume; however, shows better coulombic efficiency. In contrast, the battery with 10 µL IL volume (Figure 4a) showed a low initial discharge capacity of ~800 mAh/g with a rapid degradation over the cycling.

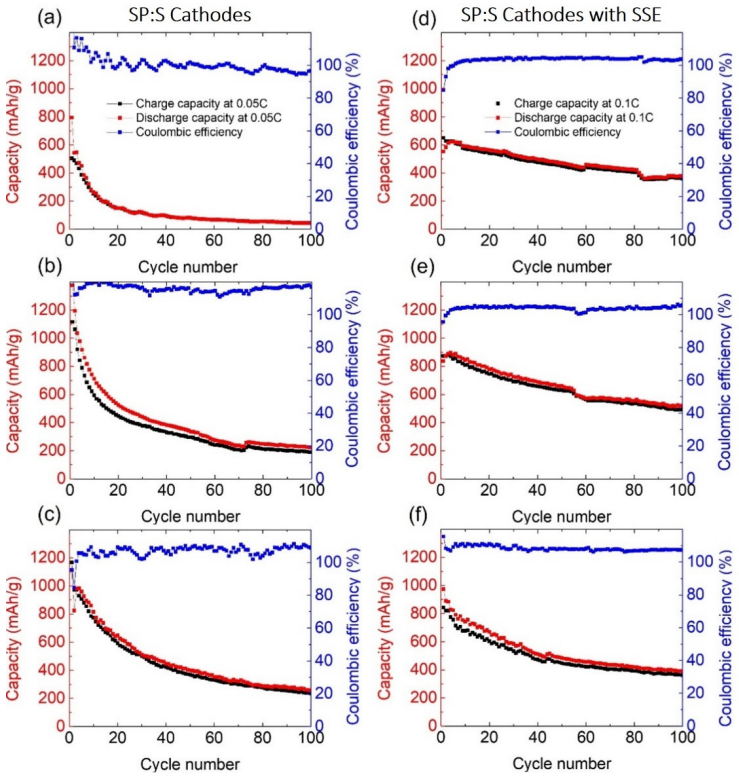

Figure 4. Performance of batteries consisting of SP–S/SSE/Li with 2 M LiTFSI PYR/DOL (1:1) with different volumes: (**a**) 10 µL, (**b**) 20 µL, (**c**) 40 µL, and performance of batteries consisting of SP–S-SSE/SSE/Li (SSE incorporated in the cathode) with 2 M LiTFSI PYR/DOL (1:1) with different volumes (**d**) 10 µL, (**e**) 20 µL and (**f**) 40 µL.

From all these studies, it was found that the functionalization of the SSE/cathode interface with an IL of 2 M LiTFSI in a diluted solution of PYR with DOL at 1:1 ratio and total volume of 40 µL gives the optimum performance.

Thereafter, the C rate dependance of the battery under optimized conditions were tested for C/20, C/10 and C/5 rates. All three batteries consist of SP-S/$Li_6PS_5F_{0.5}Cl_{0.5}$ SSE/Li with added ionic liquid of 2 M LiTFSI in a 1:1 ratio of PYR/DOL with a total volume of 40 µL. Figure S4 in the Supplementary Materials sheet shows the C rate performance results. Among all the QSSEBs tested at optimum conditions, the battery tested at C/5 stands out with its significant performance at a higher current rate. This result confirmed that the improved cathode, IL, and SSE together are capable of handling higher currents with stable coulombic efficiency and capacity.

Since the poor interface contact between the SSE and the cathode hinders the Li+ ion transport, an addition of a small amount of SSE into the cathode material is expected to improve the lithium-ion transport and hence, the capacity retention. For this reason, during the SP–S cathode formulation, a pre-determined amount of SSE was incorporated to enhance the ionic conductivity of the cathode. Specifically, $Li_6PS_5F_{0.5}Cl_{0.5}$ was dissolved in anhydrous ethanol (1 wt%) and drop casted onto the C–S cathode. Then, an IL volume-dependent study was carried out with 10, 20, and 40 µL volumes of IL and C/10 current rate. Figure 4d–f show the battery performances with SSE in the SP–S cathode at C/10 rate. As shown in Figure 4a–c, the batteries without the SSE in the SP–S cathode showed the higher initial discharge capacity but with lower retention after 100 cycles. However, after the incorporation of $Li_6PS_5F_{0.5}Cl_{0.5}$ in the C–S cathode, even if the initial capacities are slightly lower, it resulted in improved capacity retentions of (a) 65%, (b) 58%, and (c) 45% after 100 cycles with stabilized coulombic efficiency even at C/10 current rate. The reduced initial discharge capacity can be due to the reduction in the electronic conductivity of the cathode after the addition of the SSE.

Subsequently, to understand the electrochemical reactions occurring at the interface while cycling, EIS measurements were carried out after discharging the cells. Figure 5 shows the Nyquist plot of the electrochemical impedance spectra of batteries consisting of a SP–S cathode, $Li_6PS_5F_{0.5}Cl_{0.5}$ SSE, and Li anode; (a) without any ionic liquid, (b) with 40 µL of LiTFSI (1 M) dissolved in PYR, and (c) with 40 µL of LiTFSI (2 M) dissolved in PYR/DOL (1:1) before and discharging after three cycles. ASSEB without any ionic liquid showed higher charge transfer resistance compared to batteries with ionic liquid due to the higher interfacial resistance resulting from poor interfacial contact. Both charge transfer and electrolyte resistances further increased after discharging, presumably due to the formation of insulating Li_2S_2 and Li_2S at the interface. The battery with LiTFSI (1 M) dissolved in PYR has also shown a significant increase in the electrolyte resistance and charge transfer resistance after discharge, suggesting the decomposition of SSE and IL (Figure 5b). However, the battery with LiTFSI (2 M) dissolved in PYR/DOL has also shown only a slight increase in both electrolyte and charge transfer resistance as shown in Figure 5c, which could be predominantly due to the formation of Li_2S after discharge. This confirms the stability of DOL-diluted IL experimentally, which will be further, explicitly discussed in the AIMD simulation results.

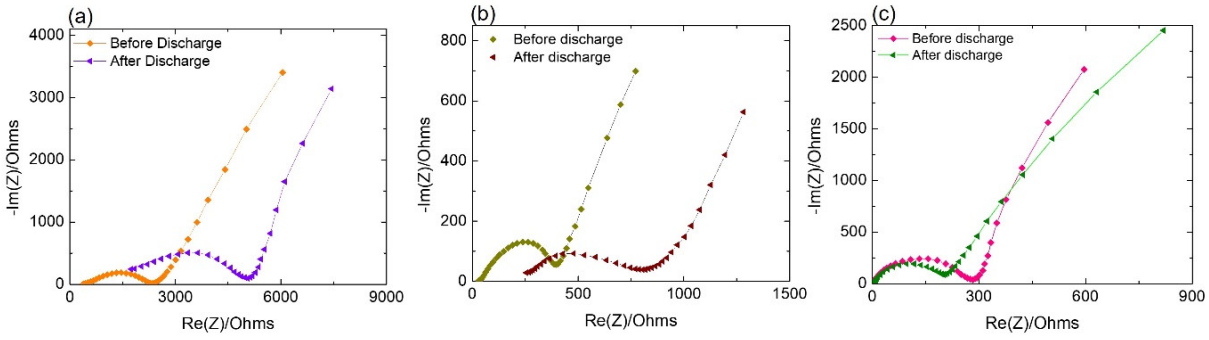

Figure 5. Electrochemical impedance spectra of batteries consisting of SP–S cathode, Li anode, and SSE (**a**) with no ionic liquid, (**b**) with IL of LiTFSI (1 M) dissolved in PYR, and (**c**) with IL of LiTFSI (2 M) dissolved in PYR/DOL (1:1) before and after discharging.

Next, cyclic voltammograms were recorded in the voltage range 1.0–2.75 V for batteries consisting of SP–S cathode, Li anode, and SSE (a) with no ionic liquid, (b) with IL LiTFSI (1 M) dissolved in PYR, and (c) with IL LiTFSI (2 M) dissolved in PYR/DOL (1:1) at scan rates of 3.0 mV/min as shown in Figure 6. Generally, at the cathode, the reduction of sulfur in liquid electrolyte Li–S batteries happens in two steps, based on the type of electrolyte utilized. The first phase is the reduction of elemental sulfur to lithium polysulfides (Li_2S_n, $2 < n < 8$) in the range of 2.4–2.1 V vs. Li/Li+, and the second phase

represents a further reduction of polysulfides to solid lithium sulfides (Li_2S_2 and Li_2S) at around 2.1–1.8 V [12,46]. In ASSEB, it is expected to have a direct conversion of elemental sulfur into solid lithium sulfides (Li_2S_2 and Li_2S). In the battery tested without any ionic liquid, the direct conversion of S_8 to solid sulfides is observed with the presence of only a single peak in the cathodic scan of around 1.8 V, as expected (Figure 6a). In comparison, QSSEBs have also shown a combined peak in the range of 2.3–1.8 V, verifying the fact that QSSEB follows more of a direct conversion route while discharging, as in ASSEB, even with the presence of ionic liquid (Figure 6b,c). Supti Das et al. have previously reported a similar cyclic voltammogram where dual cathodic peaks were seen to combine into a single reduction peak in an all-solid-state LiS battery [47]. According to their work, the difference in the areas under curve in cathodic and anodic scans in ASSEB is believed to be due to the higher scan rates employed. In contrast, compared to this work, they used much lower currents to test the battery while using a higher sweeping rate for the CV measurements. During the anodic scan, an oxidation peak, which was attributed to the conversion of lithium sulfides to elemental sulfur and lithium, was observed at 2.5 V and 2.7 V, respectively. This shows a shift from 2.4 V in the liquid electrolyte Li–S batteries [31]. The reduction and oxidation peaks did not vary significantly during cycling, confirming that a stable cathode–electrolyte interface (CEI) was formed.

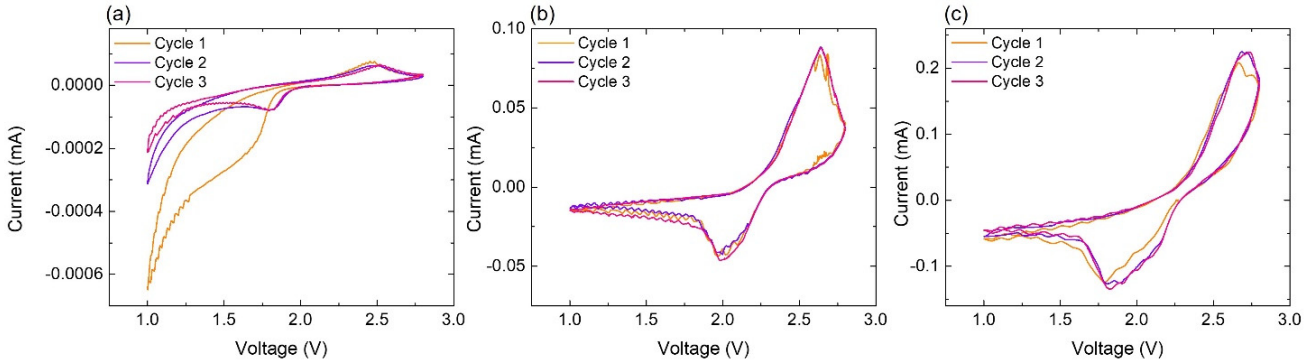

Figure 6. Cyclic voltammogram of the batteries consist of SP–S cathode, Li anode, and SSE (**a**) with no ionic liquid (**b**) with IL LiTFSI (1 M) dissolved in PYR, and (**c**) with IL LiTFSI (2 M) dissolved in PYR/DOL (1:1).

3.3. XPS Results

Figure 7 shows the XPS S2p low binding energy (BE) peak of the cathode–SSE interface of three batteries: (a) without any ionic liquid at the interfaces, (b) with the ionic liquid LiTFSI (1 M) dissolved in PYR, and in (c) and (d), with the ionic liquid LiTFSI (2 M) dissolved in PYR/DOL (1:1). XPS S2p high binding energy peaks for the batteries with ionic liquid after 100 cycles are included in the Supplementary Materials (Figure S6). All batteries were characterized after complete discharge to 1.0 V. The battery shown in Figure 7a lasted only for single cycle (see Figure 2b) due to its poor interfacial contact and displayed only the characteristic peaks corresponding to PS_4^{3-} and P_2S_5 species of the SSE. The battery shown in Figure 7b, which consisted of highly viscous IL LiTFSI (1 M) dissolved in PYR, charged/discharged for 100 cycles with very low capacity and showed an additional doublet corresponding to terminal/bridging sulfur from long chain Li-polysulfides. However, due to the low material utilization along with poor discharge capacity, peaks corresponding to the final discharge product of Li_2S were not detected in either of these batteries.

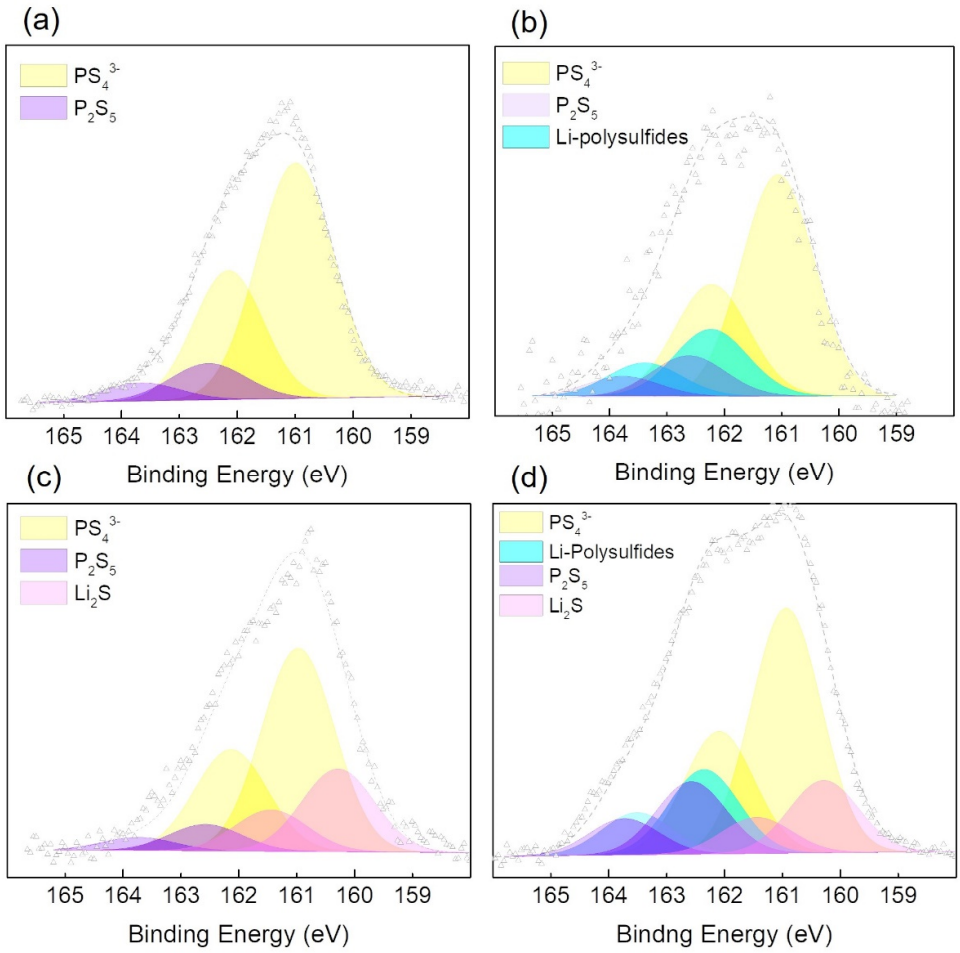

Figure 7. XPS S2p low binding energy peak of the cathode–SSE interface of (**a**) no ionic liquid, (**b**) with LiTFSI (1 M) dissolved in PYR, and (**c**,**d**) with LiTFSI (2 M) dissolved in PYR/DOL (1:1) after 1 cycle and 100 cycles.

Figure 7c,d show XPS results corresponding to the batteries with DOL diluted ionic liquid after a single cycle (c) and 100 cycles (d). In both cases, characteristic peaks for SSE (PS_4^{3-} and P_2S_5) were detected with the Li_2S peaks. Both batteries have shown significantly high initial discharge capacities confirming the presence of the Li_2S peak as the final discharge product. After 100 cycles, XPS peaks related to terminal/bridging sulfur from long-chain polysulfides were also detected in the battery. With the presence of SSE, the reaction path has less long-chain polysulfides and hence, the existence of polysulfides is expected to result mostly from the liquid electrolyte reaction path resulting from ionic liquid. After prolonged cycling, part of the polysulfides formed could have been dissolved into the ionic liquid and deposited at the SSE/cathode interface, degrading the cyclability and lowering the capacity. The failure of the battery with LiTFSI (1 M) in PYR, in comparison to the success of the battery with LiTFSI (2 M) in PYR/DOL (1:1), even though both of them show polysulfide peaks in XPS, can be understood as being due to lower polysulfide dissolution in diluted ionic liquid. In prior research conducted by Meisner Q.J. et al. [30], the improved capacity retention of ionic liquid-based liquid electrolyte batteries consisting of LiTFSI-PYR diluted with DOL due to their lower polysulfide dissolution has been shown. The XPS S2p high binding energy peak shown in Figure S5 in the Supplementary Materials shows dominant peaks corresponding to $TFSI^-$ anions from LiTFSI (solid) and PYR14-TFSI (liquid) for both batteries [47,48]. Peaks corresponding to SO_2 were detected, presumably due to the decomposition of TFSI anions resulting from both LiTFSI and PYR14-TFSI. The additional peaks corresponding to sulfates (SO_4^{2-}) are assumed to be due to the reaction of sulfides with any residual oxygen. The AIMD simulation results also show a partial

decomposition of PYR-TFSI in the 1 M LiTFSI dissolved in PYR, producing stable SO_2 and -SO_2* radicals that could also lead to the formation of SO_4^{2-}. This speculation is further confirmed with the AIMD simulation results showing improved stability in IL consisting of LiTFSI (2 M) in PYR/DOL (1:1) over LiTFSI (1 M) in PYR. However, there is no clear distinction in the XPS results of SO_2 and SO_4^{2-} between the batteries with and without DOL, since SO_2 and SO_4^{2-} can be formed from both LiTFSI and PYR-TFSI.

3.4. AIMD Simulation Results

We used AIMD simulations to gain fundamental insights into the interfacial chemical reactions that occur between (i) 2 M LiTFSI in DOL:DME (1:1), (ii) ([PYR_{14}][TFSI]), and (iii) 2 M LiTFSI in ([PYR_{14}][TFSI]):DOL (1:1), with $Li_6PS_5F_{0.5}Cl_{0.5}$ (SSE) as well as cathode states (Li_2S and S_8). Careful analysis of AIMD trajectories revealed that none of the functionalizing liquids react with the SSE (Figures S7a,b, 8a,b and 9a,b). Note, at the DOL:DME | | SSE, the ethereal oxygen of DOL and DME coordinate with Li from SSE, but without any reaction (Figure S7a,b). Similarly, no reaction was observed at any of the interfaces with the cathode in the fully charged state, i.e., S_8 (Figures S7c,d, 8c,d and 9c,d). This shows that the functionalizing liquid merely wets the cathode (fully charged), and the SSE. In contrast, the cathode in fully discharged state (Li_2S) exhibits much higher reactivity with the functionalizing liquid, primarily due to the Li atoms present in Li_2S (Figures S7e,f, 8e,f and 9e,f). At the interface between 2 M LiTFSI in DOL:DME (1:1) and Li_2S, approximately 50% of the [TFSI] anions became dissociated, forming CF_2O and -SO-N-SO_2-CF_3 species (Figure S8a). Additionally, ~20% of DME underwent decomposition, resulting in the formation of -O-CH_2-CH_2-O-CH_3 and -CH_3 species (Figure S8b). This observation aligns with the existing literature, highlighting DME's low LUMO energy levels in the presence of Li-ions [49]. Notably, although previous works state that DOL should also decompose against Li-ion via ring opening, such processes were not evident within the limited time scales accessible to AIMD simulations [49–51]. Consistent with the finding of solvent decomposition, the SP-S battery with active material loading of 0.7 $mgcm^{-2}$ using 2 M LiTFSI in DOL:DME (1:1) failed to charge back after the initial discharge cycle in our experiments (Figure S8c). On the other hand, at the interface between [PYR_{14}][TFSI] and Li_2S-cathode, 33.3% of [TFSI] dissociated into CF_3, SO_2, -CN,-SO_2 and LiF species (Figure 8g), while the [PYR_{14}] cations remains intact throughout the AIMD trajectory (Figure 8e,f). Similarly, at the 2 M LiTFSI in ([PYR_{14}][TFSI]):DOL (1:1) | | Li_2S interface, both [PYR_{14}] cations and DOL remain intact, while ~25% of [TFSI] dissociated (Figure 9e,f). Thus, in the interfaces with [PYR_{14}][TFSI] (i.e., with or without LiTFSI salt), dissociation of [TFSI] yield LiF, which is known to stabilize the interface [52,53]; consistent with good cyclability despite a rapid capacity reduction over several cycles, indicated by experiments (Figures 3 and 4). Note, in the presence of LiTFSI salt, there is amorphization of Li_2S, correlating with a slight capacity reduction in our electrochemical experiments. In both cases, where DOL-DME and ([PYR14][TFSI]) were in contact with Li2S-cathode, the dissociation of [TFSI] anions resulted in the release of fluoride ions. These fluoride ions subsequently migrated into the Li2S cathode and contributed to the formation of lithium fluoride (LiF) at the interface. (Figures 8g and S8a).

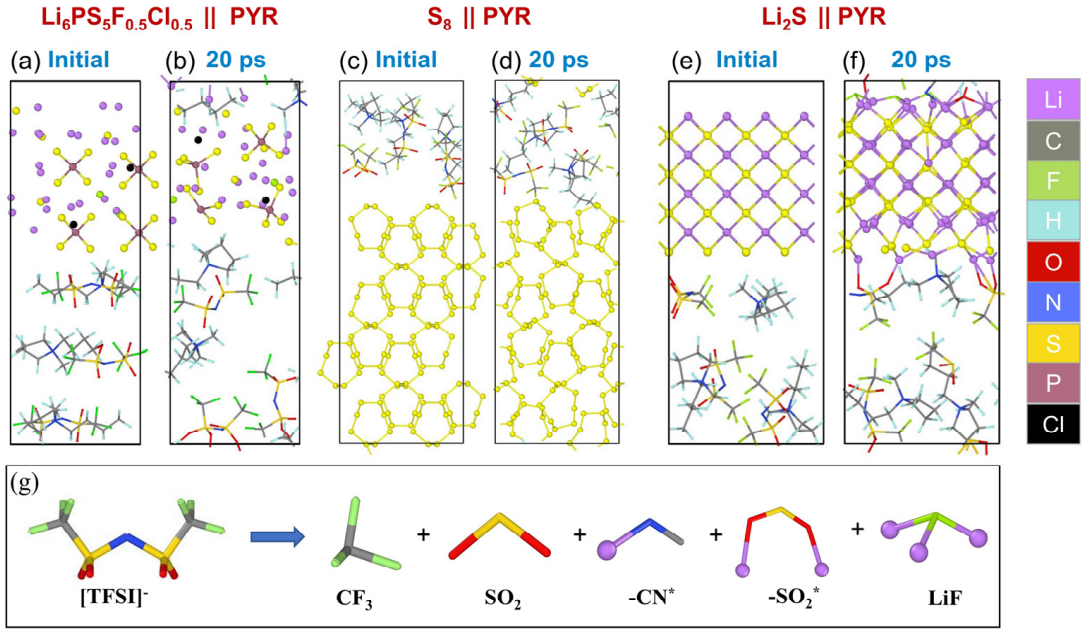

Figure 8. Structural evolution of PYR (PYR14TFSI) interface with (**a**,**b**) $Li_6PS_5F_{0.5}Cl_{0.5}$, (**c**,**d**) S8, and (**e**,**f**) Li2S obtained from ab initio molecular dynamics simulations (20 ps) under ambient conditions. (**g**) [TFSI]–decomposition products present at the end of simulation time (* represents the complexes).

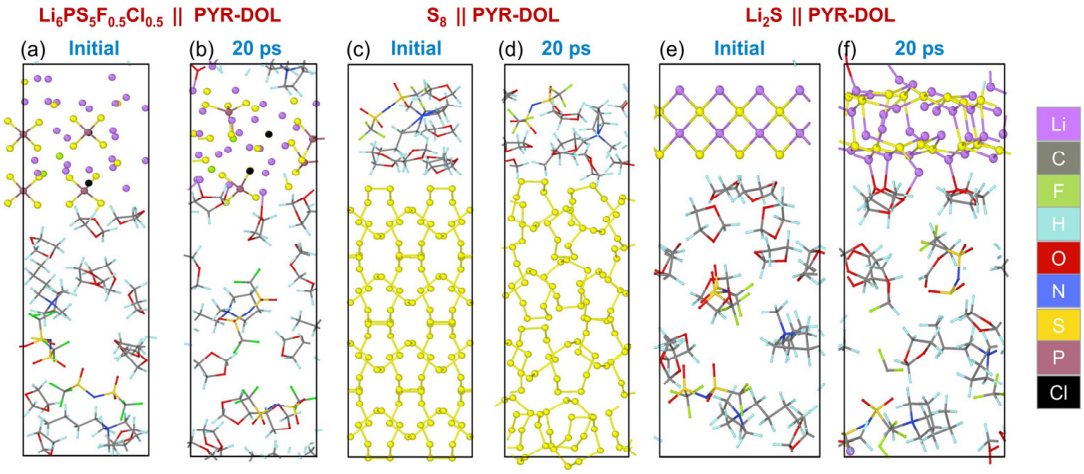

Figure 9. Structural evolution of 2 M LiTFSI in PYR (PYR14TFSI):DOL (1:1) interface with (**a**,**b**) $Li_6PS_5F_{0.5}Cl_{0.5}$, (**c**,**d**) S8, and (**e**,**f**) Li2S obtained from ab initio molecular dynamics simulations (20 ps) under ambient conditions.

4. Conclusions

Quasi-solid-state electrolyte Li–S batteries consisting of Super P–Sulfur composite cathodes, Li anodes, and novel $Li_6PS_5F_{0.5}Cl_{0.5}$ SSE were successfully developed with the use of the ionic liquid LiTFSI (2 M) dissolved in PYR:DOL (1:1) as the wetting agent at both electrode–SSE interfaces. Under optimum conditions, QSSEB batteries showed an initial discharge capacity of >1100 mAh/g and a discharge capacity of >400 mAh/g after 100 cycles at the C rate of C/10 with excellent coulombic efficiency. The volumes of IL used at the SSE–electrolyte interfaces are low enough to warrant that our QSSEBs follow solid-state Li–S reaction pathways rather than liquid electrolyte Li–S reaction routes, as confirmed by the cyclic voltammetry studies. Electrochemical stability at the cathode–SSE interface of QSSEBs was carefully investigated using the AIMD simulation studies for different ionic liquid compositions and was found to be in good agreement with the

experimental results. An IL concentration of 40 µL of LiTFSI (2 M) dissolved in PYR:DOL (1:1) was found to be optimum for high-performance QSSEBs, as verified both theoretically and experimentally. Overall understanding of the underlying chemistry of the IL in QSSEBs and the interfacial reactions at the SSE–electrode interfaces will open up new opportunities to develop high-performance, safe, and high-energy-density solid-state batteries employing sulfide-based SSEs in the near future.

Supplementary Materials: The following supporting information can be downloaded at: https://www.mdpi.com/article/10.3390/batteries10050155/s1, Figure S1: Parts of the CR2032 coin cell assembly and cross section of cathode/SSE/Li metal interface with thin layer of ionic liquids; Figure S2: Performance of QSSEB with ionic liquid LiTFSI(1M) in PYR; Figure S3: Performance of QSSEB with ionic liquid LiTFSI (1M) in PYR:DOL (1:1); Figure S4: C rate dependent cyclic performance at (a) C/20, (b) C/10, (c) C/5 rates and charge discharge curves at (d) C/20, (e) C/10, (f) C/5 for batteries consist of SP-S/SSE/Li with 40 µL of IL LiTFSI(2M) PYR:DOL(1:1); Figure S5: Cyclic voltammogram for batteries with and without ionic liquids; Figure S6: XPS S2p high BE peak of the cathode-SSE interface of 2 batteries containing (a) LiTFSI(1M) in PYR and (b) LiTFSI(2M) in PYR:DOL (1:1) after discharge of 100 cycles; Figure S7: Structural evolution of DOL:DME (1:1) interface with (a) $Li_6PS_5F_{0.5}Cl_{0.5}$, (b) S_8, and (c) Li_2S obtained from ab initio molecular dynamics simulations under ambient conditions; Figure S8: The decomposition sequence of (a) $[TFSI]^-$ and (b) DME molecules for DOL:DME (1:1) interface with Li_2S obtained from ab initio molecular dynamics simulations under ambient conditions (* represents the complexes), and (c) discharge curve of DOL:DME (1:1) IL based battery which did not charge back.

Author Contributions: Conceptualization, A.T., B.N., H.W., G.U.S. and J.B.J.; data curation, M.K.K., V.S., W.R.A., S.A., A.T., B.N., H.W., G.U.S. and J.B.J.; formal analysis, M.K.K., V.S., W.R.A., S.A., A.T., B.N., H.W., G.U.S. and J.B.J.; funding acquisition, A.T., B.N., H.W., G.U.S. and J.B.J.; investigation, M.K.K., V.S., W.R.A., S.A., A.T., B.N., H.W., G.U.S. and J.B.J.; methodology, M.K.K., V.S., W.R.A., S.A., A.T., B.N., H.W., G.U.S. and J.B.J.; project administration, B.N.; resources, A.T., B.N., H.W., G.U.S. and J.B.J.; software, V.S. and B.N.; supervision, B.N., H.W., G.U.S. and J.B.J.; validation, M.K.K., V.S., W.R.A., S.A., A.T., B.N., H.W., G.U.S. and J.B.J.; visualization, M.K.K., V.S., W.R.A., S.A., A.T., B.N., H.W., G.U.S. and J.B.J.; writing—original draft, M.K.K., V.S., W.R.A., S.A., A.T., B.N., H.W., G.U.S. and J.B.J.; writing—review and editing, M.K.K., V.S., W.R.A., S.A., A.T., B.N., H.W., G.U.S. and J.B.J. All authors have read and agreed to the published version of the manuscript.

Funding: This research was funded by U.S. Department of Energy's Office of Energy Efficiency and Renewable Energy Grant under the Vehicle Technologies Office Award No. DE-EE0008866.

Data Availability Statement: Data is contained within the article or Supplementary Materials.

Acknowledgments: The authors thank the support from U.S. Department of Energy's Office of Energy Efficiency and Renewable Energy Grant under the Vehicle Technologies Office Award No. DE-EE0008866. We also acknowledge support from the Conn Center for Renewable Energy Research at University of Louisville. This research used resources of the National Energy Research Scientific Computing Center, a DOE Office of Science User Facility supported by the Office of Science of the U.S. Department of Energy under Contract No. DE-AC02-05CH11231 (V.S., B.N.)

Conflicts of Interest: The authors declare no conflict of interest.

References

1. Armand, M.; Tarascon, J.M. Building better batteries. *Nature* **2008**, *451*, 652–657. [CrossRef] [PubMed]
2. Balakumar, K.; Kalaiselvi, N. High sulfur loaded carbon aerogel cathode for lithium–sulfur batteries. *RSC Adv.* **2015**, *5*, 34008–34018. [CrossRef]
3. Wang, S.; Zhang, Y.; Zhang, X.; Liu, T.; Lin, Y.H.; Shen, Y.; Li, L.; Nan, C.W. High-conductivity argyrodite Li6PS5Cl solid electrolytes prepared via optimized sintering processes for all-solid-state lithium–sulfur batteries. *ACS Appl. Mater. Interfaces* **2018**, *10*, 42279–42285. [CrossRef] [PubMed]
4. Bruce, P.G.; Freunberger, S.A.; Hardwick, L.J.; Tarascon, J.M. Li–O_2 and Li–S batteries with high energy storage. *Nat. Mater.* **2012**, *11*, 19–29. [CrossRef]
5. Seh, Z.W.; Sun, Y.; Zhang, Q.; Cui, Y. Designing high-energy lithium–sulfur batteries. *Chem. Soc. Rev.* **2016**, *45*, 5605–5634. [CrossRef]

6. Yang, X.; Li, X.; Adair, K.; Zhang, H.; Sun, X. Structural design of lithium–sulfur batteries: From fundamental research to practical application. *Electrochem. Energy Rev.* **2018**, *1*, 239–293. [CrossRef]
7. Zhang, S.; Ueno, K.; Dokko, K.; Watanabe, M. Recent advances in electrolytes for lithium–sulfur batteries. *Adv. Energy Mater.* **2015**, *5*, 1500117. [CrossRef]
8. Manthiram, A.; Fu, Y.; Chung, S.H.; Zu, C.; Su, Y.S. Rechargeable lithium-sulfur batteries. *Chem. Rev.* **2014**, *114*, 11751–11787. [CrossRef] [PubMed]
9. Yin, Y.X.; Xin, S.; Guo, Y.G.; Wan, L.J. Lithium–sulfur batteries: Electrochemistry, materials, and prospects. *Angew. Chem. Int. Ed.* **2013**, *52*, 13186–13200. [CrossRef]
10. Barchasz, C.; Molton, F.; Duboc, C.; Leprêtre, J.C.; Patoux, S.; Alloin, F. Lithium/sulfur cell discharge mechanism: An original approach for intermediate species identification. *Anal. Chem.* **2012**, *84*, 3973–3980. [CrossRef]
11. Mikhaylik, Y.V.; Akridge, J.R. Polysulfide shuttle study in the Li/S battery system. *J. Electrochem. Soc.* **2004**, *151*, A1969. [CrossRef]
12. Ai, W.; Zhou, W.; Du, Z.; Chen, Y.; Sun, Z.; Wu, C.; Zou, C.; Li, C.; Huang, W.; Yu, T. Nitrogen and phosphorus co-doped hierarchically porous carbon as an efficient sulfur host for Li-S batteries. *Energy Storage Mater.* **2017**, *6*, 112–118. [CrossRef]
13. Jung, D.S.; Hwang, T.H.; Lee, J.H.; Koo, H.Y.; Shakoor, R.A.; Kahraman, R.; Jo, Y.N.; Park, M.-S.; Choi, J.W. Hierarchical porous carbon by ultrasonic spray pyrolysis yields stable cycling in lithium–sulfur battery. *Nano Lett.* **2014**, *14*, 4418–4425. [CrossRef] [PubMed]
14. Gao, X.; Sun, Q.; Yang, X.; Liang, J.; Koo, A.; Li, W.; Liang, J.; Wang, J.; Li, R.; Holness, F.B.; et al. Toward a remarkable Li-S battery via 3D printing. *Nano Energy* **2019**, *56*, 595–603. [CrossRef]
15. Bauer, I.; Thieme, S.; Brückner, J.; Althues, H.; Kaskel, S. Reduced polysulfide shuttle in lithium–sulfur batteries using Nafion-based separators. *J. Power Sources* **2014**, *251*, 417–422. [CrossRef]
16. Liang, C.; Dudney, N.J.; Howe, J.Y. Hierarchically structured sulfur/carbon nanocomposite material for high-energy lithium battery. *Chem. Mater.* **2009**, *21*, 4724–4730. [CrossRef]
17. Yang, Y.; Zheng, G.; Cui, Y. Nanostructured sulfur cathodes. *Chem. Soc. Rev.* **2013**, *42*, 3018–3032. [CrossRef]
18. Quartarone, E.; Mustarelli, P. Electrolytes for solid-state lithium rechargeable batteries: Recent advances and perspectives. *Chem. Soc. Rev.* **2011**, *40*, 2525–2540. [CrossRef]
19. Manthiram, A.; Yu, X.; Wang, S. Lithium battery chemistries enabled by solid-state electrolytes. *Nat. Rev. Mater.* **2017**, *2*, 16103. [CrossRef]
20. Linford, R.G.; Hackwood, S. Physical techniques for the study of solid electrolytes. *Chem. Rev.* **1981**, *81*, 327–364. [CrossRef]
21. Sakuda, A.; Hayashi, A.; Tatsumisago, M. Sulfide solid electrolyte with favorable mechanical property for all-solid-state lithium battery. *Sci. Rep.* **2013**, *3*, 2261. [CrossRef] [PubMed]
22. Bachman, J.C.; Muy, S.; Grimaud, A.; Chang, H.-H.; Pour, N.; Lux, S.F.; Paschos, O.; Maglia, F.; Lupart, S.; Lamp, P.; et al. Inorganic solid-state electrolytes for lithium batteries: Mechanisms and properties governing ion conduction. *Chem. Rev.* **2016**, *116*, 140–162. [CrossRef] [PubMed]
23. Yu, X.; Bi, Z.; Zhao, F.; Manthiram, A. Polysulfide-shuttle control in lithium-sulfur batteries with a chemically/electrochemically compatible NASICON-type solid electrolyte. *Adv. Energy Mater.* **2016**, *6*, 1601392. [CrossRef]
24. Yu, X.; Bi, Z.; Zhao, F.; Manthiram, A. Hybrid lithium–sulfur batteries with a solid electrolyte membrane and lithium polysulfide catholyte. *ACS Appl. Mater. Interfaces* **2015**, *7*, 16625–16631. [CrossRef] [PubMed]
25. Busche, M.R.; Drossel, T.; Leichtweiss, T.; Weber, D.A.; Falk, M.; Schneider, M.; Reich, M.-L.; Sommer, H.; Adelhelm, P.; Janek, J. Dynamic formation of a solid-liquid electrolyte interphase and its consequences for hybrid-battery concepts. *Nat. Chem.* **2016**, *8*, 426–434. [CrossRef] [PubMed]
26. Liang, J.; Luo, J.; Sun, Q.; Yang, X.; Li, R.; Sun, X. Recent progress on solid-state hybrid electrolytes for solid-state lithium batteries. *Energy Storage Mater.* **2019**, *21*, 308–334. [CrossRef]
27. Shi, C.; Alexander, G.V.; O'Neill, J.; Duncan, K.; Godbey, G.; Wachsman, E.D. All-solid-state garnet type sulfurized polyacrylonitrile/lithium-metal battery enabled by an inorganic lithium conductive salt and a bilayer electrolyte architecture. *ACS Energy Lett.* **2023**, *8*, 1803–1810. [CrossRef]
28. Yang, X.; Luo, J.; Sun, X. Towards high-performance solid-state Li–S batteries: From fundamental understanding to engineering design. *Chem. Soc. Rev.* **2020**, *49*, 2140–2195. [CrossRef] [PubMed]
29. Shin, J.H.; Cairns, E.J. N-Methyl-(n-butyl) pyrrolidinium bis (trifluoromethanesulfonyl) imide-LiTFSI–poly (ethylene glycol) dimethyl ether mixture as a Li/S cell electrolyte. *J. Power Sources* **2008**, *177*, 537–545. [CrossRef]
30. Meisner, Q.J.; Rojas, T.; Glossmann, T.; Hintennach, A.; Liu, Q.; Cao, J.; Redfern, P.C.; Ngo, A.T.; Curtiss, L.A.; Zhang, Z. Impact of co-solvent and LiTFSI concentration on ionic liquid-based electrolytes for Li-S battery. *J. Electrochem. Soc.* **2020**, *167*, 070528. [CrossRef]
31. Dharmasena, R.; Thapa, A.K.; Hona, R.K.; Jasinski, J.; Sunkara, M.K.; Sumanasekera, G.U. Mesoporous TiO_2 coating on carbon–sulfur cathode for high capacity Li–sulfur battery. *RSC Adv.* **2018**, *8*, 11622–11632. [CrossRef] [PubMed]
32. Su, Y.S.; Fu, Y.; Manthiram, A. Self-weaving sulfur–carbon composite cathodes for high rate lithium–sulfur batteries. *Phys. Chem. Chem. Phys.* **2012**, *14*, 14495–14499. [CrossRef] [PubMed]
33. Singhal, R.; Chung, S.H.; Manthiram, A.; Kalra, V. A free-standing carbon nanofiber interlayer for high-performance lithium–sulfur batteries. *J. Mater. Chem. A* **2015**, *3*, 4530–4538. [CrossRef]

34. Ma, L.; Zhuang, H.L.; Wei, S.; Hendrickson, K.E.; Kim, M.S.; Cohn, G.; Hennig, R.G.; Archer, L.A. Enhanced Li–S batteries using amine-functionalized carbon nanotubes in the cathode. *ACS Nano* **2016**, *10*, 1050–1059. [CrossRef] [PubMed]
35. Li, H.; Wang, J.; Zhang, Y.; Wang, Y.; Mentbayeva, A.; Bakenov, Z. Synthesis of carbon coated Fe_3O_4 grown on graphene as effective sulfur-host materials for advanced lithium/sulfur battery. *J. Power Sources* **2019**, *437*, 226901. [CrossRef]
36. Li, T.; Bo, H.; Cao, H.; Lai, Y.; Liu, Y.; Huang, Z. Effects of carbon hosts on electrochemical properties of lithium-sulfur batteries. *Int. J. Electrochem. Sci.* **2017**, *12*, 5731–5741. [CrossRef]
37. Cho, I.; Choi, J.; Kim, K.; Ryou, M.H.; Lee, Y.M. A comparative investigation of carbon black (Super-P) and vapor-grown carbon fibers (VGCFs) as conductive additives for lithium-ion battery cathodes. *RSC Adv.* **2015**, *5*, 95073–95078. [CrossRef]
38. Zheng, C.; Wang, K.; Li, L.; Huang, H.; Liang, C.; Gan, Y.; He, X.; Zhang, W.; Zhang, J. High-Performance All-Solid-State Lithium–Sulfur Batteries Enabled by Slurry-Coated Li6PS5Cl/S/C Composite Electrodes. *Front. Energy Res.* **2021**, *8*, 606494. [CrossRef]
39. Chen, Y.; Li, W.; Sun, C.; Jin, J.; Wang, Q.; Chen, X.; Zha, W.; Wen, Z. Sustained release-driven formation of ultrastable sei between Li6PS5Cl and lithium anode for sulfide-based solid-state batteries. *Adv. Energy Mater.* **2021**, *11*, 2002545. [CrossRef]
40. Fan, X.; Ji, X.; Han, F.; Yue, J.; Chen, J.; Chen, L.; Deng, T.; Jiang, J.; Wang, C. Fluorinated solid electrolyte interphase enables highly reversible solid-state Li metal battery. *Sci. Adv.* **2018**, *4*, eaau9245. [CrossRef]
41. Kresse, G.; Furthmüller, J. Efficiency of ab-initio total energy calculations for metals and semiconductors using a plane-wave basis set. *Comput. Mater. Sci.* **1996**, *6*, 15–50. [CrossRef]
42. Jain, A.; Ong, S.P.; Hautier, G.; Chen, W.; Richards, W.D.; Dacek, S.; Cholia, S.; Gunter, D.; Skinner, D.; Ceder, G.; et al. Commentary: The Materials Project: A materials genome approach to accelerating materials innovation. *APL Mater.* **2013**, *1*, 011002. [CrossRef]
43. Arnold, W.; Shreyas, V.; Li, Y.; Koralalage, M.K.; Jasinski, J.B.; Thapa, A.; Sumanasekera, G.; Ngo, A.T.; Narayanan, B.; Wang, H. Synthesis of Fluorine-Doped Lithium Argyrodite Solid Electrolytes for Solid-State Lithium Metal Batteries. *ACS Appl. Mater. Interfaces* **2022**, *14*, 11483–11492. [CrossRef] [PubMed]
44. Grimme, S.; Ehrlich, S.; Goerigk, L. Effect of the damping function in dispersion corrected density functional theory. *J. Comput. Chem.* **2011**, *32*, 1456–1465. [CrossRef]
45. Kumaresan, K.; Mikhaylik, Y.; White, R.E. A mathematical model for a lithium–sulfur cell. *J. Electrochem. Soc.* **2008**, *155*, A576. [CrossRef]
46. Das, S.; Ngene, P.; Norby, P.; Vegge, T.; de Jongh, P.E.; Blanchard, D. All-Solid-State Lithium-Sulfur Battery Based on a Nanoconfined $LiBH_4$Electrolyte. *J. Electrochem. Soc.* **2016**, *163*, A2029–A2034. [CrossRef]
47. Shen, Z.; Zhong, J.; Xie, W.; Chen, J.; Ke, X.; Ma, J.; Shi, Z. Effect of LiTFSI and LiFSI on cycling performance of lithium metal batteries using thermoplastic polyurethane/halloysite nanotubes solid electrolyte. *Acta Metall. Sin. (Engl. Lett.)* **2021**, *34*, 359–372. [CrossRef]
48. Nandasiri, M.I.; Camacho-Forero, L.E.; Schwarz, A.M.; Shutthanandan, V.; Thevuthasan, S.; Balbuena, P.B.; Mueller, K.T.; Murugesan, V. In situ chemical imaging of solid-electrolyte interphase layer evolution in Li–S batteries. *Chem. Mater.* **2017**, *29*, 4728–4737. [CrossRef]
49. Chen, X.; Hou, T.-Z.; Li, B.; Yan, C.; Zhu, L.; Guan, C.; Cheng, X.-B.; Peng, H.-J.; Huang, J.-Q.; Zhang, Q. Towards stable lithium-sulfur batteries: Mechanistic insights into electrolyte decomposition on lithium metal anode. *Energy Storage Mater.* **2017**, *8*, 194–201. [CrossRef]
50. Shi, C.; Takeuchi, S.; Alexander, G.V.; Hamann, T.; O'Neill, J.; Dura, J.A.; Wachsman, E.D. High Sulfur Loading and Capacity Retention in Bilayer Garnet Sulfurized-Polyacrylonitrile/Lithium-Metal Batteries with Gel Polymer Electrolytes. *Adv. Energy Mater.* **2023**, *13*, 2301656. [CrossRef]
51. Liu, Q.; Cresce, A.; Schroeder, M.; Xu, K.; Mu, D.; Wu, B.; Shi, L.; Wu, F. Insight on lithium metal anode interphasial chemistry: Reduction mechanism of cyclic ether solvent and SEI film formation. *Energy Storage Mater.* **2019**, *17*, 366–373. [CrossRef]
52. Merinov, B.V.; Zybin, S.V.; Naserifar, S.; Morozov, S.; Oppenheim, J.; Goddard, W.A., III; Lee, J.; Lee, J.H.; Han, H.E.; Choi, Y.C.; et al. Interface structure in Li-metal/[Pyr14][TFSI]-ionic liquid system from ab initio molecular dynamics simulations. *J. Phys. Chem. Lett.* **2019**, *10*, 4577–4586. [CrossRef] [PubMed]
53. Li, Y.; Halacoglu, S.; Shreyas, V.; Arnold, W.; Guo, X.; Dou, Q.; Jasinski, J.B.; Narayanan, B.; Wang, H. Highly efficient interface stabilization for ambient-temperature quasi-solid-state sodium metal batteries. *Chem. Eng. J.* **2022**, *434*, 134679. [CrossRef]

Disclaimer/Publisher's Note: The statements, opinions and data contained in all publications are solely those of the individual author(s) and contributor(s) and not of MDPI and/or the editor(s). MDPI and/or the editor(s) disclaim responsibility for any injury to people or property resulting from any ideas, methods, instructions or products referred to in the content.